Processing of the 2018 CaMI VSP survey for full waveform inversion

Matt Eaid, Scott Keating, and Kris Innanen

ABSTRACT

In 2018, the Consortium for Research in Elastic Wave Exploration Seismology in partnership with the Containment and Monitoring Institute (CaMI) acquired a vertical seismic profile using three-component accelerometers and distributed acoustic sensing fibers. The overarching goal of CaMI is to develop technologies for the monitoring of sequestered CO_2 in a reservoir at 300 meters depth using time-lapse seismic methods. The 2018 VSP was a acquired as a baseline survey to support these goals. In this report, both the accelerometer and DAS datasets are processed to prepare them for inclusion in full waveform inversion. FWI of these two datasets will be discussed in two companion reports in this issue.

INTRODUCTION

Climate change is one of the most significant challenges that Earth faces. The consensus of the scientific community that the main driver for climate change is the anthropogenic release of greenhouse gases (Rodhe, 1990; Oreskes, 2004; Cook et al., 2013; Kweku et al., 2017). As these gases are generated, they rise into the atmosphere where they linger, trap heat from the sun, destabilize the global climate. Left unchecked, these greenhouse gases are expected to trap increasingly more energy from the sun, which is projected to lead to more frequency and severe weather patterns across Earth. Carbon dioxide (CO_2), produced as a by-product of combustion, is a particularly prolific green house gas.

Carbon capture and storage (CCS) is an area of research aimed at reducing the effect of atmospheric CO_2 by diverting it away from the atmosphere during industrial processes using a capture technology. The captured CO_2 is then transported (typically by pipeline) to a field site where it is injected into reservoirs for long term storage. A major concern for CCS is the possibility for CO_2 to escape from the desired reservoir, accumulate in near surface reservoirs, and then escape into the atmosphere. This would negate the benefits of CCS, and has the potential for a sudden and catastrophic release of carbon dioxide that could create significant health problems for people in the immediate vicinity.

The development of technologies for monitoring injected CO_2 is a key goal of many CCS projects. Ideally, these technologies would allow for the tracking of the plume over time, ensuring it remains in the target reservoir, and allowing for the detection of leaks before they become a significant problem. Seismic monitoring is a key technology for facilitating the safe storage of CO_2 in deep subsurface reservoirs. Using seismic monitoring for CCS projects involves collection of a baseline seismic survey prior to fluid injection, and recurring monitor surveys after various stages of fluid injection. If the same seismic acquisition is used for the baseline and monitor surveys, and minimal seasonal variation occurs in the near surface, then changes in the seismic data between surveys will be related to the injected CO_2. The variation in the seismic data can be used to track its location, extent, and its properties, allowing seismic monitoring to provide a high resolution image of the injected fluid.

The Containment and Monitoring Institute (CaMI) under Carbon Management Canada (CMC) focuses on the development of technologies for monitoring injected carbon dioxide at its Field Research Station in Brooks, Alberta. The goal of the FRS is the development of methods for monitoring the growth of a CO_2 plume maintained in the water filled Basal Belly River sandstone unit of Upper Cretaceous age at a depth of 300 meters (Isaac and Lawton, 2016). To facilitate this goal, a vertical seismic profile (VSP) baseline survey was acquired in 2018 using accelerometers and collocated distributed acoustic sensing (DAS) fiber in a monitoring well located approximately 20 meters southwest of the injector well. In this report, the accelerometer data, and DAS data are processed in order to prepare them for inclusion in full waveform inversion which will be reported on in two companion reports (Keating et al., 2021; Eaid et al., 2021).

CONTAINMENT AND MONITORING INSTITUTE FIELD RESEARCH STATION: 2018 VSP SURVEY

The chief goal of the Containment and Monitoring Institutes Field Research Station (located near Brooks, Alberta see Figure 1) is the development of technologies and processes for monitoring CO_2 sequestered in the late Cretaceous Basal Belly River Sandstone at 300 meters depth (Lawton et al., 2018; Macquet et al., 2019; Spackman, 2019). Amongst the proposed technologies for realizing this goal, seismic monitoring is projected to be a key tool for imaging of the CO_2 plume. To support seismic monitoring many acquisition tools have been deployed at the field research station (FRS). The FRS houses three wells, including the well being used for CO_2 injection, and two observation wells. Observation well 2, colloquially referred two as the geophysics well permanently houses a straight DAS fiber, and a helically wound fiber with a lead angle of 30° This report focuses on processing data acquired with the straight DAS fiber, and data acquired with 296 Inova VectorSeis, three-component accelerometers that were temporarily deployed in the geophysics well for the duration of the VSP acquisition program.

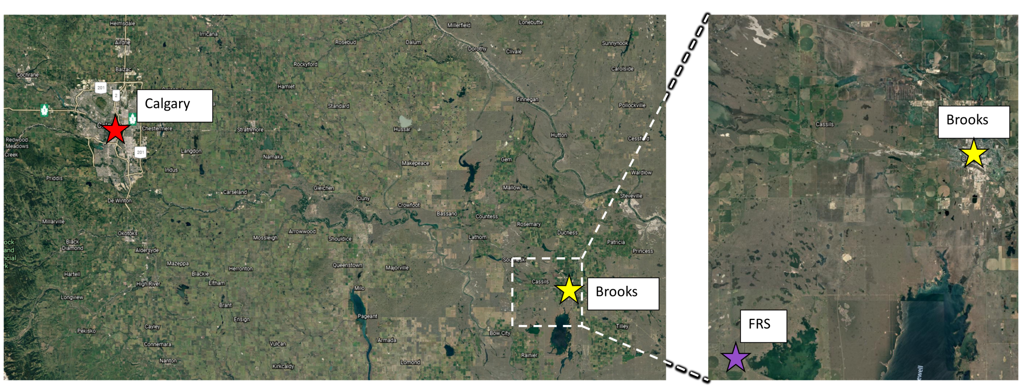

FIG. 1. Location of the CaMI FRS in Newell Country, in relation to Calgary, Alberta, and Brooks, Alberta.

Data were generated with an Inova Geophysical® UniVib with a linear sweep from 1-150 Hz over 16 seconds, using 0.2 second half cosine tapers and a 3 second listening time. Figure 2a plots the Klauder wavelet computed through an auto-correlation of the sweep, and Figure 2b plots the amplitude spectrum of the wavelet in Figure 2a. Shot points were centered on observation well 2 on 12 shot lines separated by 15° (see Figure 3). Shot lines 1, 4, 7, and 10 have a 10 meter shot spacing, and the remaining lines have 60 meter shot spacing (marked by the concentric circles in Figure 3). Missing shots on each line are result of surface obstructions at the field site. The data generated using the sweep in Figure 2 and the shot geometry in Figure 3 were acquired with 296 levels of accelerometers, and straight and helical DAS fiber in observation well 2. This report will detail the processing required to prepare the accelerometer and straight DAS fiber data for FWI.

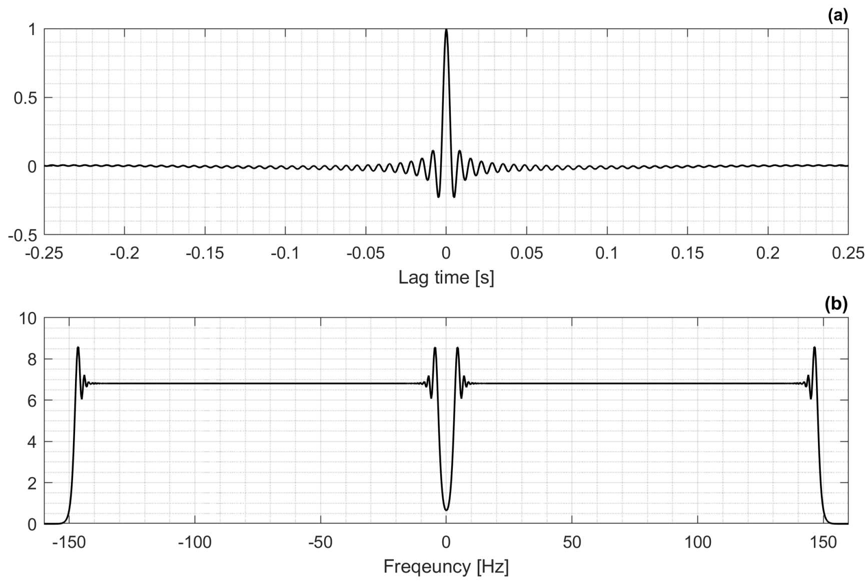

FIG. 2. (a) Klauder wavelet computed through auto-correlation of the sweep, and (b) its corresponding amplitude spctrum.

FIELD DATA PROCESSING

Field data in their raw form are often not a suitable input for FWI algorithms. Coherent noise, amplitude differences between the data and modeling, incoherent noise, and other challenges associated with field data can combine to cause poor FWI model updates. To cope with this, the field data must be processed to make it more suitable for FWI. Generally, the goal when processing field data for FWI is to only process the data to such an extent that it is a sufficiently close match to the modeled data so that the data matching in FWI can be successful. The DAS and accelerometer data, will follow a similar overall processing workflow, but due to inherent differences in the two sensor types, each dataset will require slightly unique processing steps. For both datasets, the focus will be on data acquired in observation well 2, generated by sources on source line 1 (the sources of interest are highlighted in blue in Figure 4).

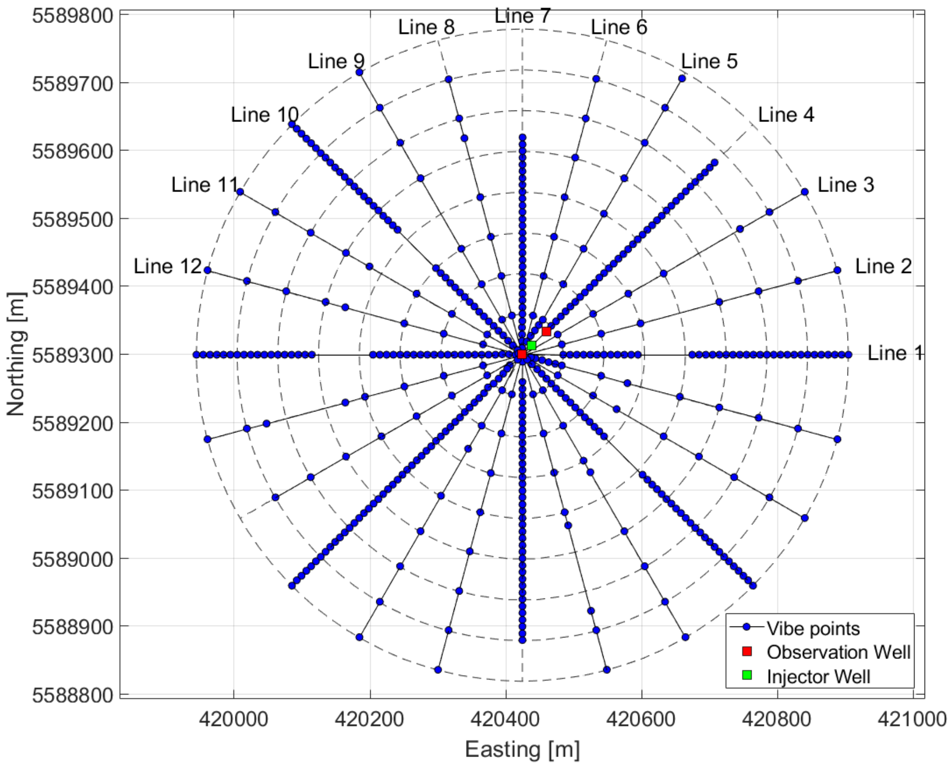

FIG. 3. Shot geometry of the CaMI-FRS 2018 3D walkaway-walkaround VSP. The blue circles represent shot point locations, the red squares the locations of the two observation wells (Observation well 2 is at the center of the shot points), and the green square the location of the injector well. The dotted lines are 60 meter concentric circles centered on observation well 2.

Accelerometer data processing

Survey Geometry

Figure 5 outlines the processing flow used to prepare the accelerometer data for full waveform inversion. The first step in the processing workflow is to initialize the geometry for the survey. During acquisition, each shot points northing and easting, as well as elevation were recorded using a global position system (GPS). The location of the well head of observation well 2 was also recorded, and the northing and easting of the accelerometers were assigned the northing and easting of the well. In reality, the well has a slight (maximum of 9°) inclination from approximately 200 meters depth to the bottom of the well as measured on the accelerometers (Hall et al., 2018). However, the azimuth of the inclination is unknown, so this is unaccounted for in the geometry and subsequent modeling. The theoretical trace spacing for the designed acquisition is 1 m, however the cable for the accelerometers is not rigid and stretches over the length of the well resulting in increasing trace spacing with depth. Additionally, as previously stated the trace spacing shifts from 1 m to 2 m at a depth of 266.4 m due to the failure of the clamping mechanism of one of the strings. Figure 6 plots the receiver depth for each accelerometer in the survey. The change in slope in Figure 6 around 266 meters depth is where the receiver spacing changes to 2 m.

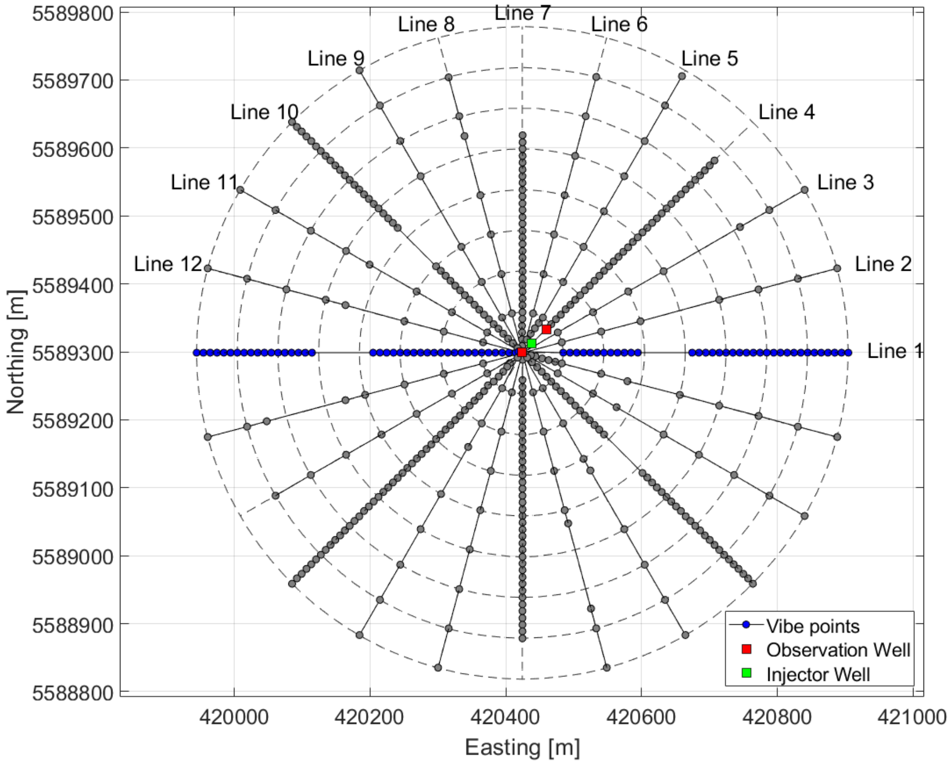

FIG. 4. Shot geometry of the CaMI-FRS 2018 3D walkaway-walkaround VSP. The blue circles represent shot point locations on source line 1, the red squares the locations of the two observation wells (Observation well 2 is at the center of the shot points), and the green square the location of the injector well. The dotted lines are 60 meter concentric circles centered on observation well 2.

Source line 1 has a maximum potential offset of 480 m on each side of observation well 2. Each shot is assigned a five digit shot point number, where the first two digits are the line number, and the last three digits are the shot number (the leading zero is eliminated for source lines 1-9). The shot on the eastern edge of this source line is shot number 101, (i.e. the eastern shot on line 1 is 1101), with the southern most shot on the N-S line 7 being given shot number 101. The shot numbers then increase for each potential 10 meter shot spacing. For example, on line 1 shot 2 is assigned shot point number 1102, whereas the second shot on line 2 is assigned shot point number 2107 because it has a 60 m shot spacing. Due to computational restrictions, the modeling used will be 2D, so I focus my attention to source line 1, consisting of shots 1101-1197. Additionally, most of the signal occurs in the first 500 ms of the dataset, so the extracted line 1 dataset is windowed to include only the first 500 ms of the 3 seconds of data.

First break picking and coordinate rotations

Figure 7 plots the raw accelerometer data for every 13^{th} shot point on source line 1 with shot points separated by vertical yellow lines, and each component separated by horizontal yellow lines. Each column plots one of the shots points, while the top row plots the vertical component, the middle row one of the two horizontal components (H_1), and the bottom row

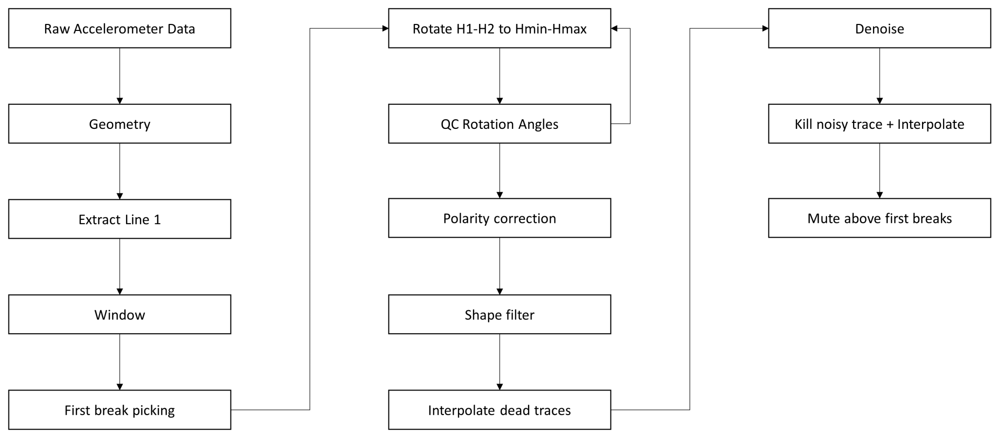

FIG. 5. Accelerometer processing workflow

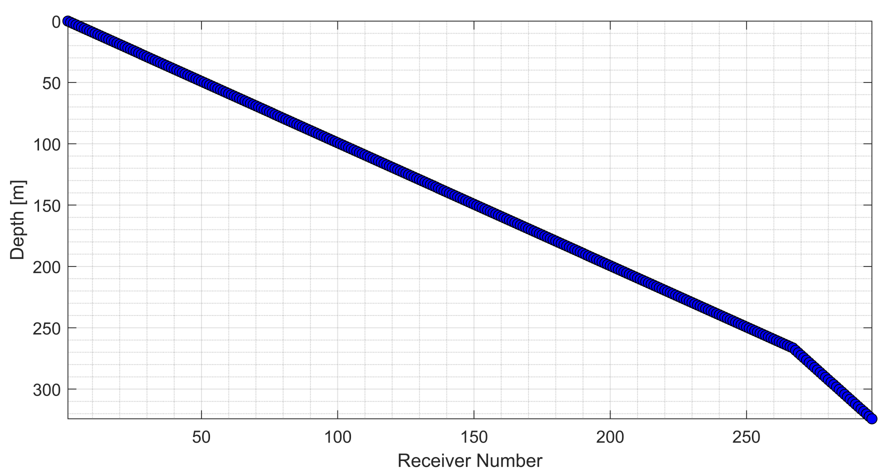

FIG. 6. Depth versus receiver number for each accelerometer used in processing and modeling.

the second horizontal component (H_2). First breaks were picked on the vertical component using the first break picking algorithm in Schlumberger's Vista processing software. The algorithm parameters were designed to search for a peak within a sliding search window around the approximate first arrivals times on each shot record. However, there is a prominent polarity reversal in the first P-wave arrival on the vertical component, that gets pushed to deeper receivers on further offset shots. It is hypothesized that this polarity reversal is caused by a diving wave arriving prior to the direct waves on shallow receivers at far offsets (Lawton, 2020). This diving wave would produce upward first motion of the accelerometer instead of the downward motion caused by a direct arrival, leading to a polarity reversal. This polarity reversal causes a $180°$ phase shift in the first breaks at a given depth. A second pass of the first break picking was done to correct for the polarity change, and to quality control erroneous first break picks. These first break picks were then transferred to the horizontal components. Figure 8 plots the same shot records as figure 7 with the quality controlled first break picks plotted in green.

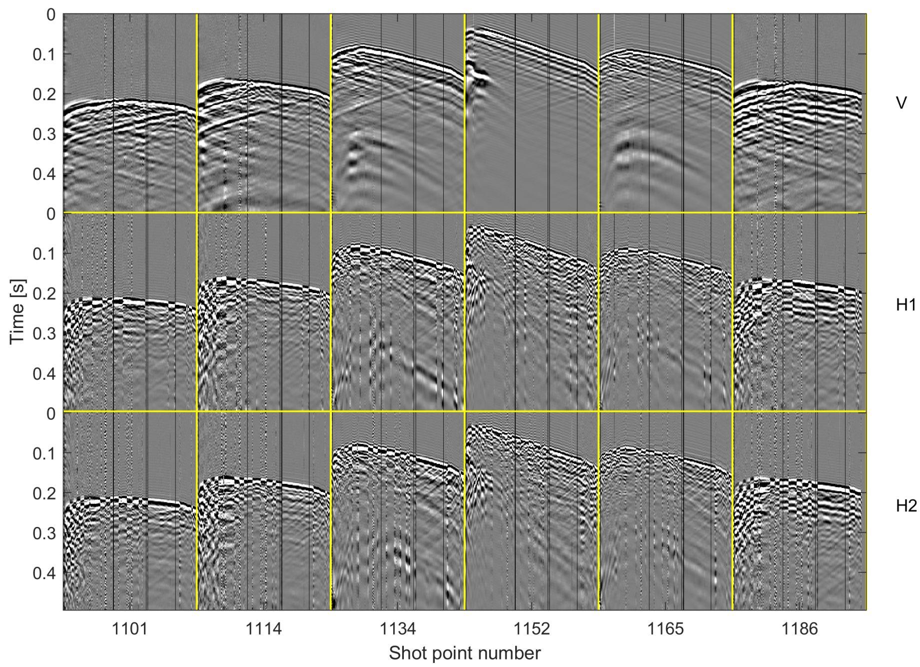

FIG. 7. Raw accelerometer data for every 13^{th} shot point on source line 1. The top row plots the vertical component, the middle row one of the horizontal components, and the bottom row the second horizontal component.

The accelerometer field data consist of the three orthogonal components of acceleration caused by the propagating wavefield, however, the horizontal components are orientated in an unknown and arbitrary direction that varies for each receiver. To ensure the horizontal data for each receiver samples a consistent azimuth, a coordinate rotation must be applied to each receiver so that the horizontal directions of each are aligned. The rotation algorithm uses a 10 ms window centered on the first break picks and calculates the rotation angles that maximize the first P-wave arrival energy on one of the horizontal components, and minimizes it on the other. The resultant components are referred to as $\mathrm{H_{max}}$ and $\mathrm{H_{min}}$, where

$$\begin{bmatrix}\mathrm{H_{max}}\\ \mathrm{H_{min}}\end{bmatrix} = \begin{bmatrix}\cos(\theta) & -\sin(\theta)\\ \sin(\theta) & \cos(\theta)\end{bmatrix}\begin{bmatrix}\mathrm{H_1}\\ \mathrm{H_2}\end{bmatrix} \tag{1}$$

and θ is computed to maximize the P-wave energy within the the search window on $\mathrm{H_{max}}$. The horizontal component that maximizes P-wave energy is the direction aligned with the horizontal component of the P-wave polarization vector, while $\mathrm{H_{min}}$ lies in the direction orthogonal to the horizontal component of the P-wave polarization vector. The direction $\mathrm{H_{max}}$ is often refereed to as the radial direction, and in an isotropic-elastic medium consists of P-$\mathrm{S_V}$ wave motion, while $\mathrm{H_{min}}$ is often refereed to as the transverse direction and consists of $\mathrm{S_H}$ wave motion.

Figure 9 plots the rotation angles required for the conversion to $\mathrm{H_{max}}$ and $\mathrm{H_{min}}$ in equa-

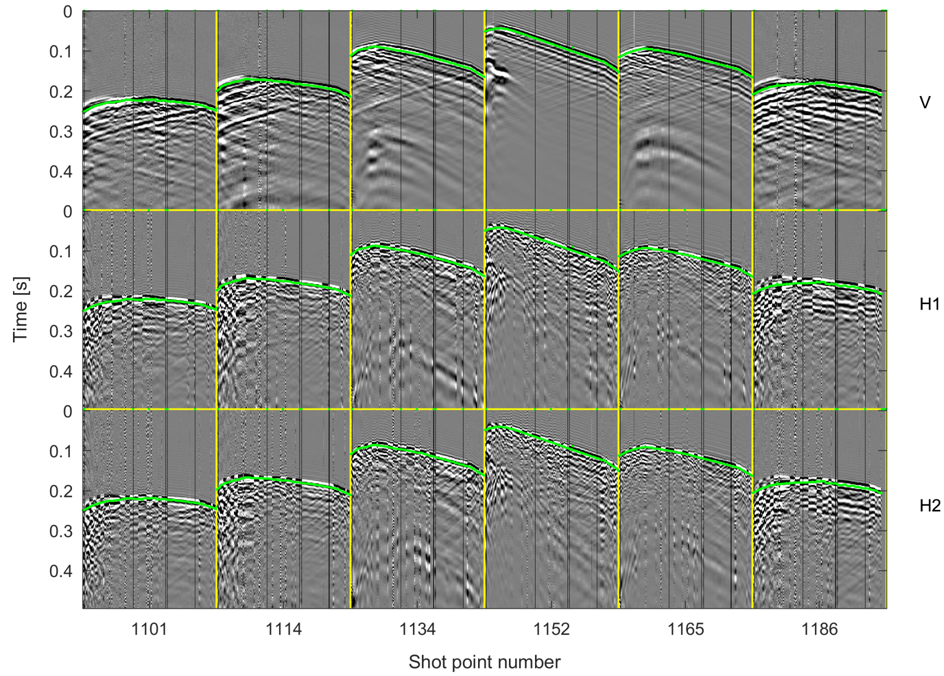

FIG. 8. Raw accelerometer data for every 13^{th} shot point on source line 1 with the first break picks plotted in green. The top row plots the vertical component, the middle row one of the horizontal components, and the bottom row the second horizontal component.

tion (1) for shot point 1186 Figure 9(a), shot point 1165 Figure 9(b), and shot point 1149 Figure 9(c) as a function of receiver depth. These shot points represent a far offset, mid-offset, and the nearest offset shot on source line 1 respectively. Figure 9(d) plots the angles for shot point 1186 in blue, shot point 1165 in red, and shot point 1149 in green. Using bow springs, the accelerometers in observation well 2 were clamped to the well casing for the duration of the VSP acquisition. Additionally, the shot points (see Figure 4) on line 1 approximately lie on a straight line passing through the well. For these two reasons, it is expected that the rotation angles for each receiver, should be approximately constant for all shot points on the same source line. This expectation holds for the rotation angles for shot points 1186 and 1165 in Figure 9(d) for all but the shallowest receivers. However, the rotation angles for shot point 1149 in Figure 9(d) deviate significantly from those computed on the other two shot points, and this error grows with depth. I hypothesize that as the shot points move closer to the observation well, a larger portion of the seismic energy is detected by the vertical component, and the horizontal components detect increasingly less energy. As this occurs, the minimization algorithm that computes the rotation angles becomes unstable, as the difference in energy on H_{min} and H_{max} becomes increasingly small. This problem is exacerbated for deeper receivers that detect less energy on their horizontal components. To combat this issue, the average rotation angles for those shots that have consistency in their rotation angles are applied to all of the shot records to rotate to H_{min} and H_{max}. This results in better data character and fewer artifacts on the near offset shots compared to the shot records using the rotations angles from Figure 9. In the 2D x-z medium that I will use for modeling, the modeled components of acceleration are directly comparable to the vertical and H_{max} components. Therefore the remainder of the processing will focus on these two components. Figure 10 plots the vertical and H_{max} accelerometer data for the same six shot points in Figure 7.

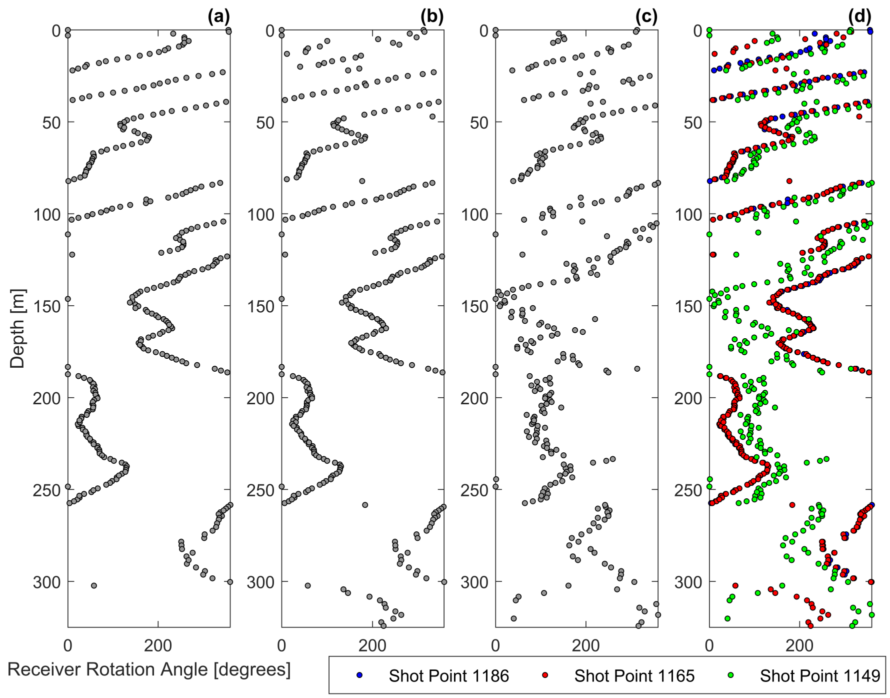

FIG. 9. Calculated rotation angles as a function of depth for (a) shot point 1186, (b) shot point 1165, and (c) shot point 1149. (d) Computed rotation angles for shot point 1186 (blue), for shot point 1165 (red), and for shot point 1149 (green).

Polarity correction

The H_{max} data are more coherent than the H_1 and H_2 datasets and consists of clear downgoing P-wave and S-wave energy, as well as reflections and mode conversions. An issue with the coordinate rotation algorithm that was used is that it is designed such that the polarity of the vertical component remains unchanged. This has clearly influenced the polarity of the horizontal component, but it appears artificial, changing from trace to trace with no zero crossing. The polarity change, that moves deeper with offset, is harder to motivate for the horizontal component. If the polarity change is caused by diving waves arriving before the direct downgoing arrivals as hypothesized, a wave that initially begins with downgoing and eastward P-wave motion, but which bends along its ray path such that the P-wave motion is upgoing at the receiver will still have an eastward directed horizontal component of P-wave motion. Assuming the hypothesis surrounding diving waves is correct, than it is expected that the polarity of the direct arrival on the H_{max} component will be constant for any given shot record. It is also expected that the polarity will flip about zero offset as the P-wave pushes the accelerometer in opposite directions for sources on each side of the well. The issue that remains is which polarity is correct for each side of the well. One option is to adopt The Society for Exploration Geophysicists (SEG) proposed conventions for the polarity of multi-component data (Krebes, 2019). Here, the first beak polarity of the P-wave data should match the polarity of modeled data, which is a trough for shots west of the observation well, and a peak for shots east of the observation well. Figure 11

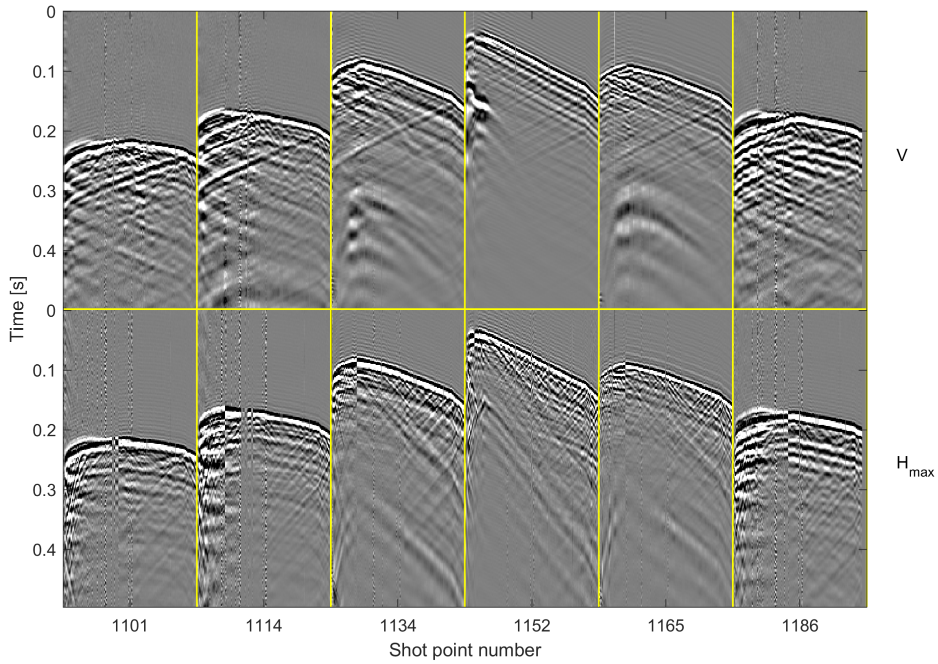

FIG. 10. Accelerometer data after coordinate rotations for every 13^{th} shot point on source line 1. The top row plots the vertical component and the bottom row the H_{max} component.

plots the same data as Figure 10 but with the polarity of the horizontal component updated to match this convention, where shot points 1149-1197 are west of the well.

Shape filtering

The data in Figure 11 contain ringing side lobe energy that is most apparent prior to the first arrivals on shot points 1152 and 1165, but is also likely to contaminate the data after the first arrivals. It is challenging to pinpoint the origin of this ringing, but one potential cause is differences in the theoretical sweep and actual ground force that the vibroseis injects which causes large side-lobe energy during the source auto-correlation step that is done in the field. Removal of this noise is important for FWI due its coherent and repetitive nature which FWI will potentially treat as signal, leading to erroneous model updates. The repetitive nature of this noise, and its hypothesized relationship to correlation makes it a strong candidate for predictive deconvolution type removal. However, all attempts at removing the noise with deconvolution were unsuccessful. Instead, a shaping filter approach was taken. Shaping filters find the filter that shapes an input wavelet to a least squares match of a desired wavelet, by solving the equation,

$$f_f = (W_0^{\mathrm{T}} W_0)^{-1} (W_0^{\mathrm{T}} W_D) \tag{2}$$

where W_0 is the input wavelet, W_D the desired wavelet, and f_f the computed filter. The desired wavelet is a compressed and less ringy version of the input wavelet that is computed from the first breaks. For the desired wavelet, I choose the theoretical Klauder wavelet from Figure 2b, and compute the input wavelet as an auto-correlation of the field data within a window around the first breaks, assuming that the field data wavelet is approximately a

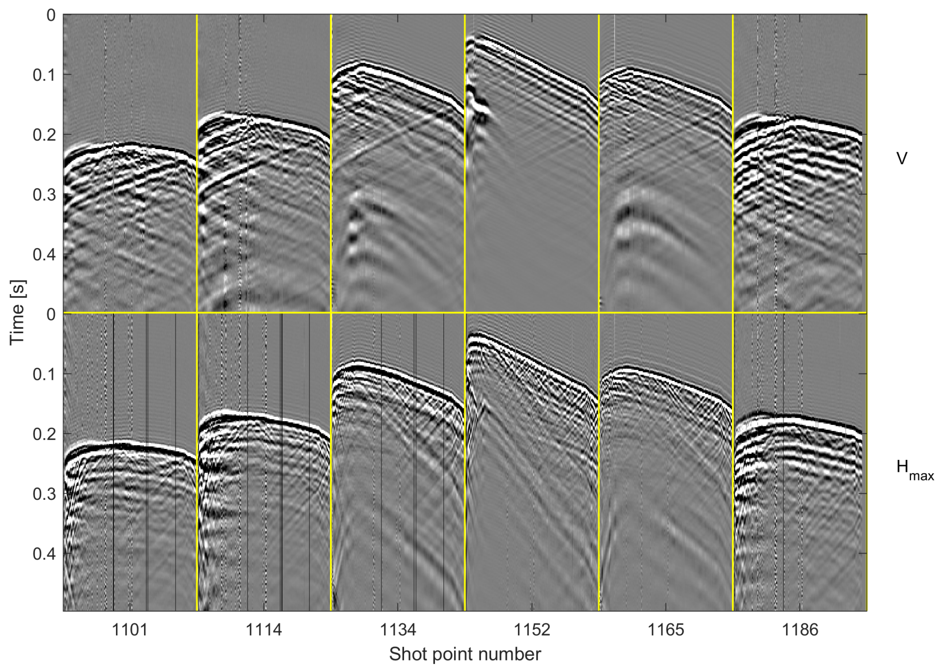

FIG. 11. Accelerometer data after coordinate rotations and manual poarity correction for every 13^{th} shot point on source line 1. The top row plots the vertical component and the bottom row the H_{max} component.

ringy version of the Klauder wavelet. Figure 12 plots the five-point shape filter computed using these two wavelets. The filter in Figure 12 was then convolved with the traces in the accelerometer dataset. Figure 13a plots the input data in row one, the data after application of the shaping filter in row two, and the difference between the two in row three. Figure 13b plots the 200th trace from the data in Figure 13a for the input data in black and the shape filtered data in red. Largely, the signal that is removed from the data after application of the shape filter consists of repetitive and ringy signal that would have been detrimental to FWI, while the beneficial data remains intact.

Noise attenuation

While these data have a relatively high signal-to-noise ratio, there are a few artifacts in the data that may present challenges for FWI. Some of the traces are consistently noisy on all of the shot records (see shot records 1114 and 1186 in Figure 11 for examples) suggesting the accelerometer is faulty either mechanically or in its coupling to the borehole. Regardless of the reason for this relatively poor signal-to-noise ratio an effort must be made to reduce the noise on these traces. Figure 11 also displays black vertical striping, which represent dead traces that have no amplitude recorded as a result of faulty hardware. Noise is another challenge that must be addressed. Gaussian noise is not typically detrimental to FWI (Lines, 2014) as the modeling algorithms used generally cannot reproduce it, and it is hard to construct model updates which generate Gaussian type noise. Coherent noise is much more detrimental to FWI. The goal in FWI is to produce a plausible model that reduces data misfit and it is fairly straight forward for FWI to introduce artifacts into the

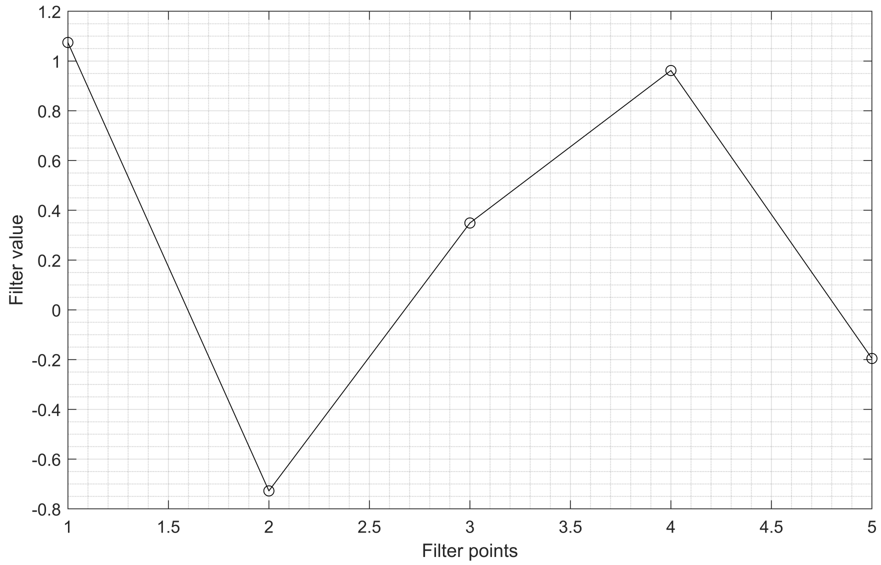

FIG. 12. Five-point shaping filter computed using an auto-correlation of the field data as the input wavelet, and a Klauder wavelet as the desired wavelet.

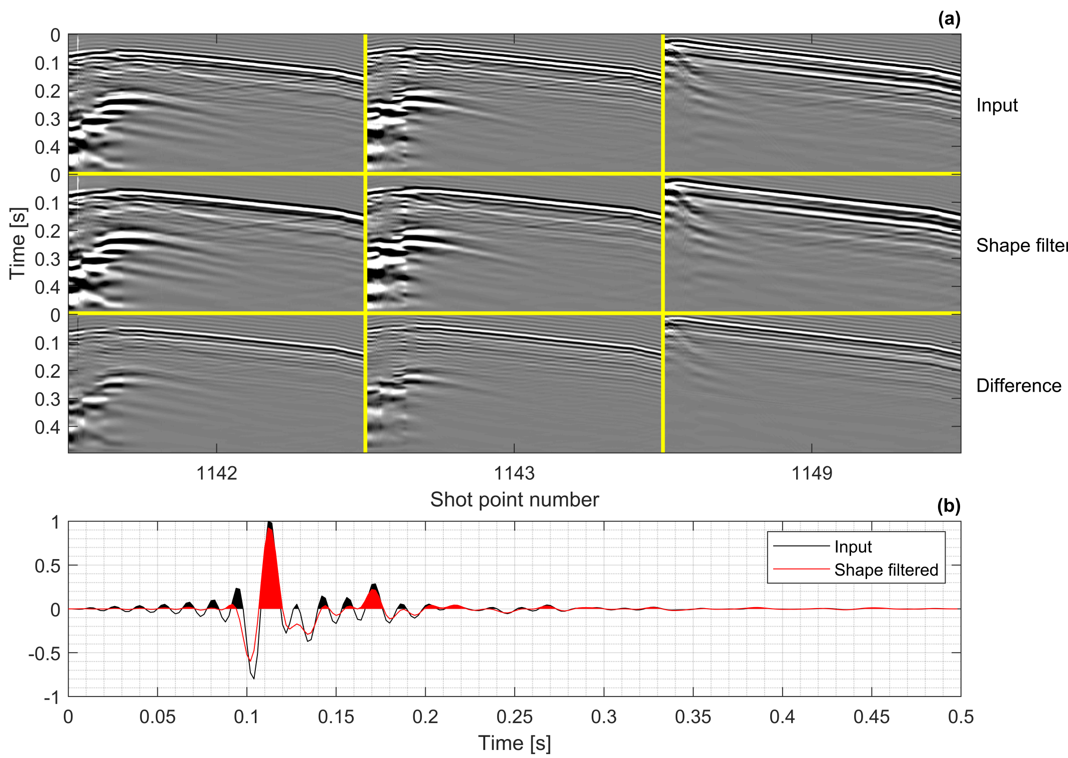

FIG. 13. (a) Accelerometer data after shape filtering for shots points 1142,1143, and 1149 on source line 1. The top row plots the vertical component of the input data, the middle row the data after shape filter application, and the bottom row the difference. (b) The 200th trace from (a) before shape filtering (black) and after shape filtering (red).

model as it attempts to reconstruct coherent noise. The dead traces are first interpolated and then a robust denoising algorithm is employed to attenuate the noise in each shot record.

A robust denoiser based on sparsity-promoting filters is employed, that preserves signal while attenuating both Gaussian, and the more challenging to remove erratic noise resulting from bad traces (Zhao et al., 2018). With sparsity-promoting filters, it is assumed that there exists a transform (i.e. the curvelet transform) to a domain over which the seismic wavefronts are sparse, but the noise is not. To denoise using this type of transform, an optimization problem is formulated

$$\hat{\mathbf{D}} = \min||\mathbf{S}_f\hat{\mathbf{D}}||_1, \qquad s.t. \qquad ||\mathbf{D}-\hat{\mathbf{D}}||_2 \leq \epsilon_n \tag{3}$$

where $\hat{\mathbf{D}}$ are the denoised data we wish to estimate, $\mathbf{D}$ are the input seismic data, $\mathbf{S}_f$ is a sparsity promoting transform, ϵ_n is proportional to the noise level, and $||*||_n$ represents the L_n norm. The optimal solution to equation (3),

$$\hat{\mathbf{D}} = \mathbf{S}_f^{\dagger} T_w \mathbf{S}_f \mathbf{D} \tag{4}$$

is the one for which the recovered data $\hat{\mathbf{D}}$ is maximally sparse, subject to the condition that recovered data are correlated to the input data within the noise level. Where T_w is the soft threshold parameter,

$$T_w(\chi) = \begin{cases} t - \text{sign}(\chi)w & |\chi| \geq w \\ 0 & |\chi| < w \end{cases} \tag{5}$$

where t are the thresholding expansion coefficients, χ are the curvelet transform coefficients, and w is a threshold parameter that depends on the noise level, and desired sparsity.

The L_2 criteria for the data fit means that this algorithm is not robust to outliers of the type present in noise bursts or overly noisy traces. A better criteria is known as the Huber criteria,

$$\rho_c(\mathbf{D}-\hat{\mathbf{D}}) = \begin{cases} 0.5(\mathbf{D}-\hat{\mathbf{D}})^2 & |\mathbf{D}-\hat{\mathbf{D}}| \leq c \\ c(|\mathbf{D}-\hat{\mathbf{D}}| - c) & |\mathbf{D}-\hat{\mathbf{D}}| > c \end{cases} \tag{6}$$

where c is a constant proportional to the standard deviation of the noise ($c = 1.345\sigma$ (e.g Zhao et al., 2018)). The criteria in equation (6) is L_2 for noise levels below approximately 1.345 times the standard deviation of the noise, but a weighted L_1 norm for larger noise levels. This allows the sparsity promoting optimization problem to be expressed as,

$$\underset{\text{argmin}\hat{\mathbf{D}}}{f_f(\hat{\mathbf{D}}|\mathbf{D})} = \rho_c(\mathbf{D}-\hat{\mathbf{D}}) + \kappa||\mathbf{S}_f\hat{\mathbf{D}}||_1 \tag{7}$$

which handles Gaussian noise similar to equation (3), but is more robust to outlier noise. I employ a similar workflow as Zhao et al. (2018) to denoise the vertical and $\mathrm{H}_{\max}$ components of the accelerometer data. Figure 14 plots the same six shot records as Figure 11 after interpolation of the dead traces, denoising using the sparsity promoting curvelet filter, and low pass filtering using a zero phase Butterworth filter with a cutoff frequency of 75 Hz.

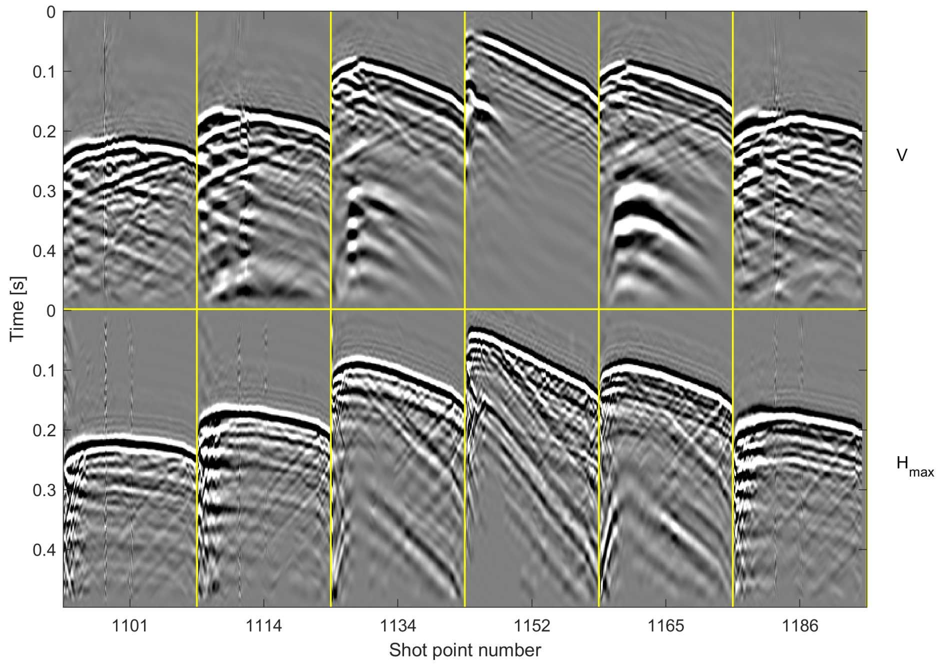

FIG. 14. Accelerometer data after trace interpolation, denoising, and low pass filtering for every 13^{th} shot point on source line 1. The top row plots the vertical component and the bottom row the H_{max} component.

After denoising and low pass filtering many of the noisy traces have been attenuated and much of the Gaussian noise has been removed. However, some noisy traces remain, and residual noise remains above the first breaks, which will be detrimental for frequency domain inversion. The residual noisy traces are muted and interpolated, and the data from time zero to 30 ms above the first breaks are muted, providing the final dataset that will be used as input for the accelerometer inversion plotted in Figure 15.

Distributed acoustic sensing data processing

Distributed acoustic sensing data are inherently different than the data supplied by more conventional multicomponent point sensors. However, many of the processing steps that were applied to the accelerometer data will also be applied to the DAS data. Figure 16 displays the processing steps that will be taken in processing the DAS data to support full waveform inversion.

Survey geometry

The processing flow in Figure 16 has the same intention as the workflow for the accelerometer data, that is, use the minimally complex processing workflow that creates data that supports full waveform inversion. The reduction from 3C to a single component reduces the need for coordinate rotations, and the cementing of the DAS fiber behind the casing results in fewer noisy and dead traces, reducing the complexity of the processing workflow. The first step is to extract shot records on source line 1 over a window of 500

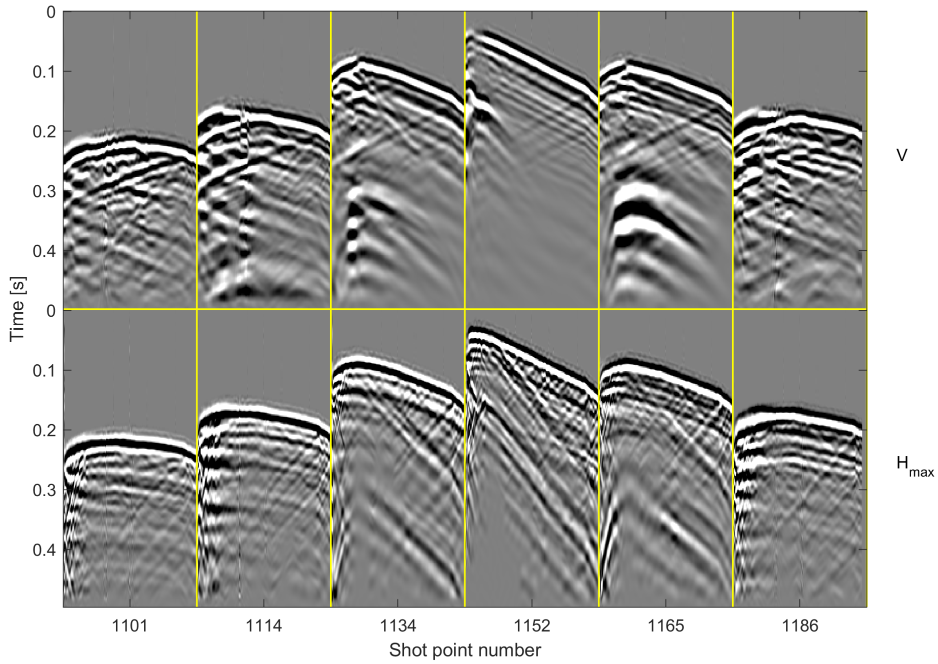

FIG. 15. Accelerometer data after following the processing workflow in Figure 5 for every 13^{th} shot point on source line 1. The top row plots the vertical component and the bottom row the H_{max} component.

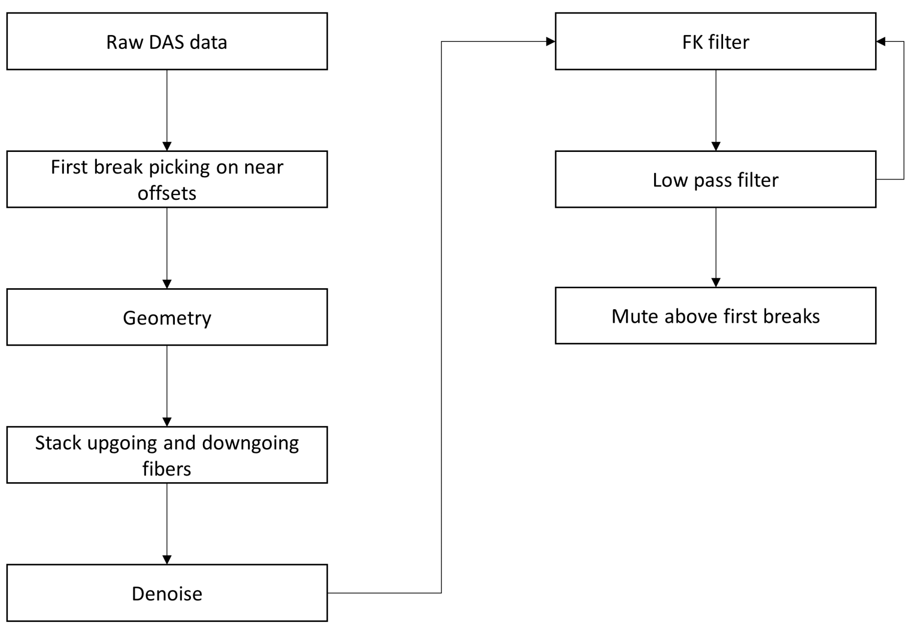

FIG. 16. Distributed acoustic sensing processing workflow

ms. Unfortunately, the interrogator unit failed to trigger for some of the shots, so the DAS dataset from source line 1 only has 64 shots, instead of the 77 shots on the accelerometer dataset. Figure 17 shows one shot record (shot number 1133) for source line 1. The DAS data comes from one 5 km interconnected loop, and consists of six distinct sections of coherent events, separated by noisy sections. These sections (from left to right) are data from the helical fiber in observation well 2, the straight fiber in observation well 2, the straight fiber in observation well 1, the northeast portion of straight fiber in the trench, the helical fiber in the trench, and finally the southwest portion of straight fiber in the trench. The noisy sections that lack signal are where the fiber runs uncoupled along the ground, or is inside junction boxes. The helical fiber has a markedly lower SNR that degrades significantly with offset so the focus will be given to the straight fiber data.

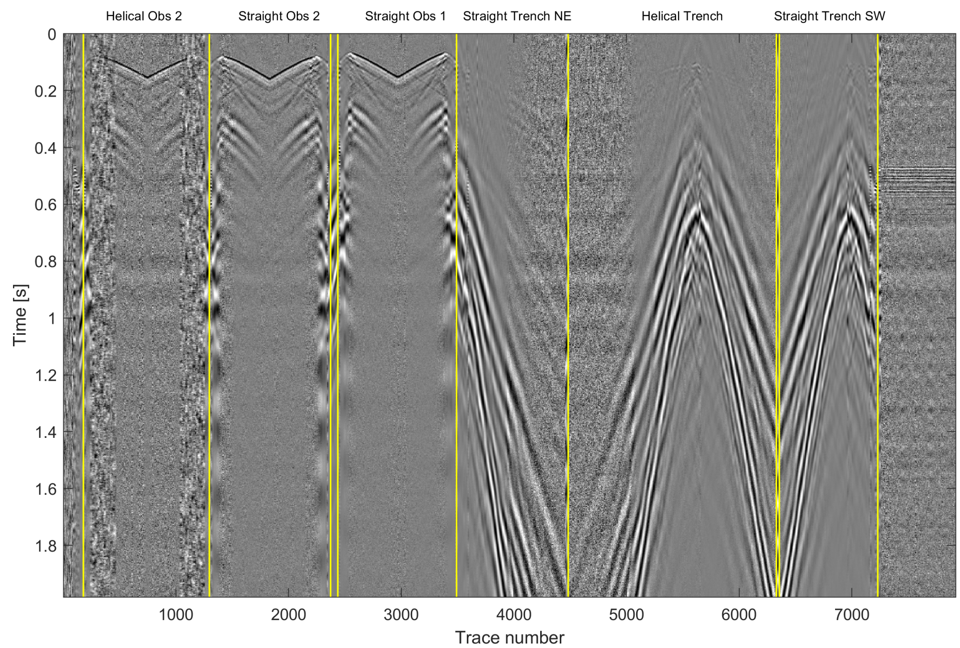

FIG. 17. DAS data from shot point 1133.

The data from the trenched fiber has good signal strength and recovers non-aliased ground roll due to the dense trace spacing, which is of significant interest in inverting for near surface velocity information (Qu and Innanen, 2021). In this report focus is directed to the fiber data that is collocated with the accelerometer data in observation well 2. The cutoffs labeled in Figure 17 are chosen manually to approximately separate the data into its six sections. Unlike point sensor data in which we have well defined sensor locations, one of the challenges associated with DAS data is that uncertainty exists in the the trace locations. This is due to 1) that a theoretical trace spacing is used that depends on interrogator parameters which may have uncertainty, and 2) that it can be challenging to spatially locate the point on the fiber containing the first trace in the well due to uncertainty and gauge length effects. The generally accepted methodology for reducing this uncertainty is to preform what is known as a tap test in which the fiber is tapped where enters the well, and the "loudest" trace on the tap test is taken as the first well-born trace. The theoretical trace spacing is then used to depth register the remaining traces. The issue with this methodology is that it is assumed that the theoretical trace spacing is accurate, and that the fiber is perfectly straight in the well. If either of these assumptions is violated, then the error in trace depth will grow with well depth.

First break picking and depth registration

Instead a data driven method is proposed in which first breaks are picked on a select number of high signal-to-noise ratio, near-offset shots from the DAS data. These first breaks are then compared to the first breaks from the same shots on the accelerometer data. For each accelerometer trace in the shot record, the DAS first break picks are compared to the first break pick from that accelerometer. The DAS trace with the best fitting first break pick is assigned the depth of that accelerometer. Figure 18 plots the shot geometry for the DAS data, with the shots used for the depth registration highlighted in blue. For each of these shot points rough boundaries for the data emanating from the straight fiber in observation well 2 were picked, and the resulting shot records were extracted. First breaks were then picked on each shot record for both the downgoing, and upgoing fiber loops in the well. Figure 19 plots the three shots used for this analysis.

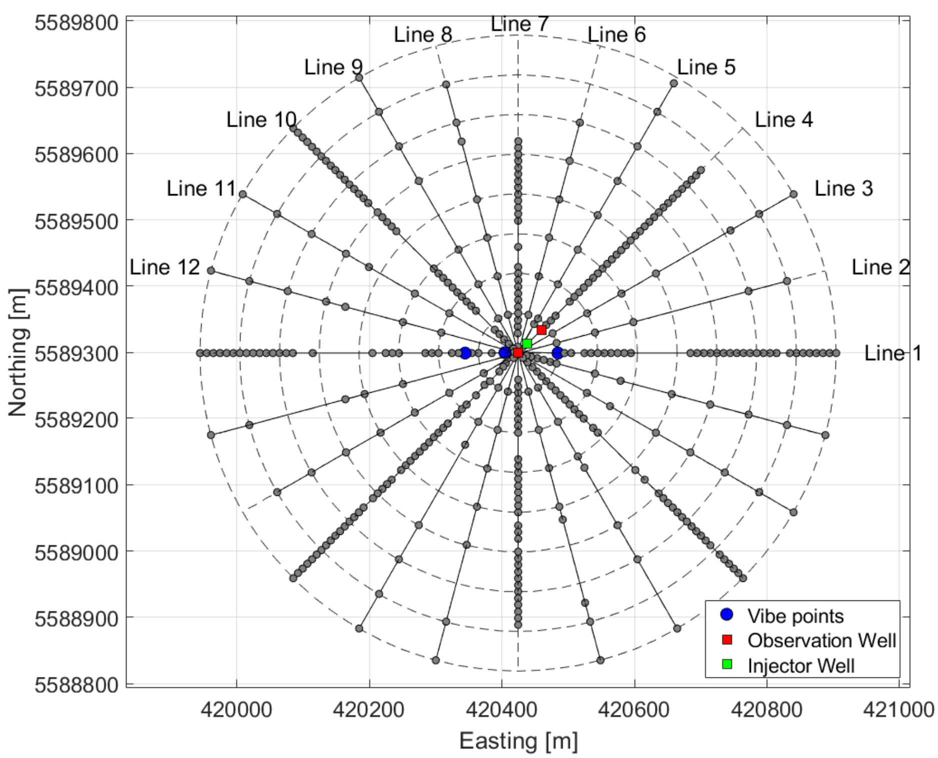

FIG. 18. Shot geometry of the CaMI-FRS 2018 3D walkaway-walkaround VSP for the DAS data. The gray circles represent shot point locations with blue circles representing shots where first breaks were picked, the red squares the locations of the two observation wells (Observation well 2 is at the center of the shot points), and the green square the location of the injector well. The dotted lines are 60 meter concentric circles centered on observation well 2.

The first break picks from these three shots were compared against the first break picks from the accelerometer shot records for the same shot point numbers. Figure 20 plots the first break picks from shot point 1142 for the accelerometer data in red and the down-

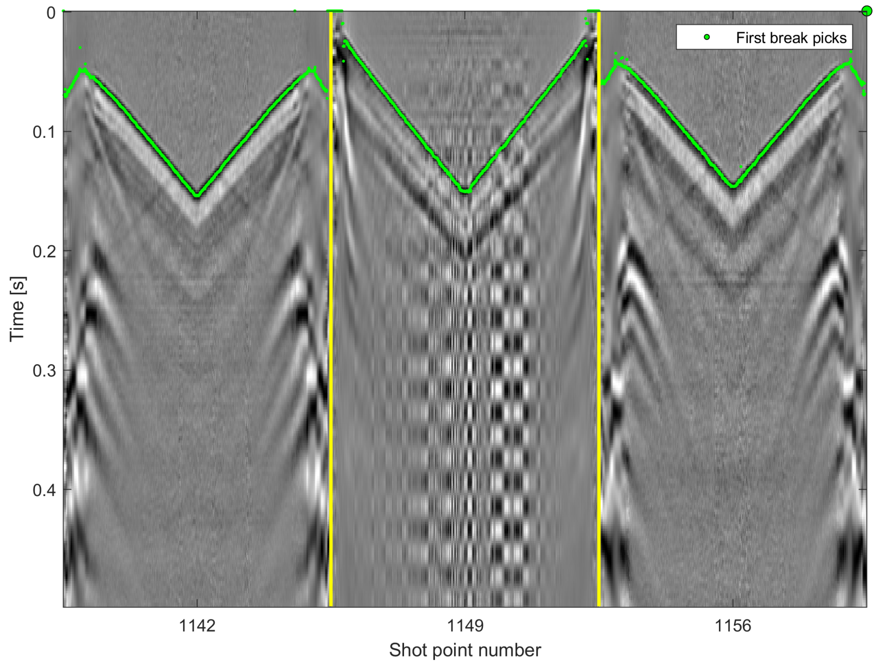

FIG. 19. The three DAS shots used for depth registration with picked first break picks plotted in green.

sampled DAS data in blue. For each red dot (representing the first break pick on a single accelerometer) the DAS trace with the first break pick that best matches the accelerometer first break pick is assigned the depth of that accelerometer. This is repeated for each of the three selected shots, and the results averaged to help mitigate the influence of small variations in the first break picks. Figures 21a and 21b plot the depth registered DAS shot records for the downgoing and upgoing straight fiber in observation well 2 for shot point 1142. The upgoing and downgoing shot records contain redundant information, so they are stacked into a single shot record to boost the signal to noise ratio of the data and plotted in Figure 21c. The stacked depth registered data compares well to the accelerometer data, suggesting that the data driven trace registration methodology successfully depth registers the DAS traces. Figure 22 plots the depth registered DAS data for every fourth shot point on source line 1.

Noise attenuation and artifact removal

One of the challenges with DAS data is its inherently lower signal-to-noise ratio. Figure 22 shows a step change in the noise level at offsets greater than approximately 200 m. There is also linear noise on many of the near offset shot records that arrives at all points on the fiber at the same time. This noise is a result of the interrogator itself shaking in the trailer due to anthropogenic activity on the surface. Noise of this type can be significantly detrimental to FWI as discussed earlier. A similar sparsity-promoting denoising algorithm is applied to the DAS data. Figure 23 plots the same data as Figure 22 after denoising with the sparsity-promoting curvelet-transform-based algorithm. The denoiser has removed the linear noise on the near offset shots, and attenuated some of the Gaussian noise. In this

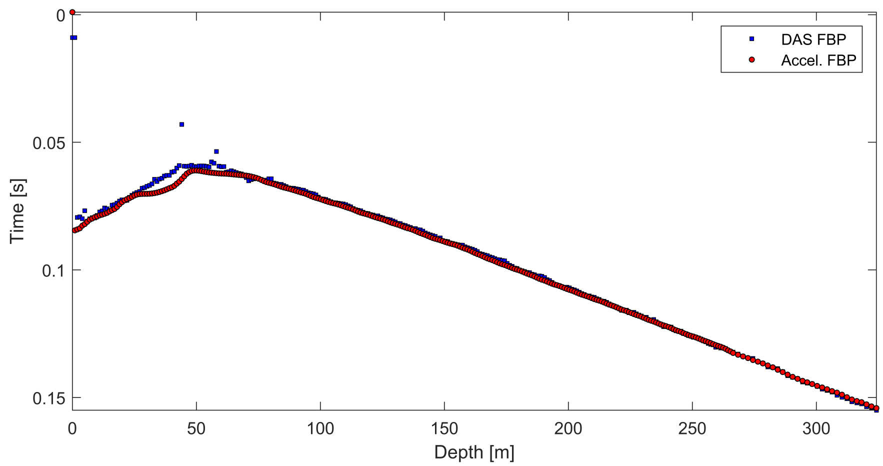

FIG. 20. First break picks from shot 1142 for the acclerometer data (red) and DAS data (blue).

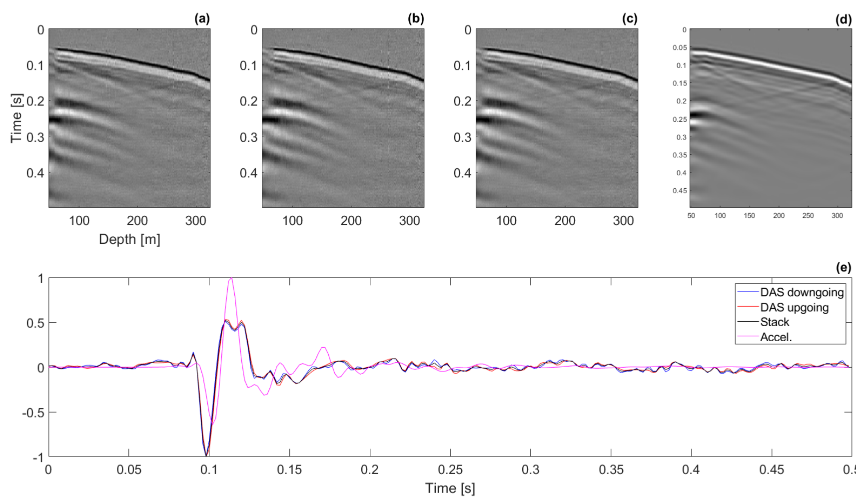

FIG. 21. Depth registered DAS data from shot point 1142 for (a) the downgoing fiber in observation well 2, (b) the upgoing fiber, and (c) the stack of the data in (a) and (b). (d) The collocated accelerometer data, (e) the trace at 200 meters depth for the downgoing fiber (blue), upgoing fiber (red), stack (black), and accelerometer data (magenta).

case, the lower signal-to-noise ratio has led to many artifacts in the denoised data, which manifest as curvelet signatures. Fortunately, many of the artifacts are more steeply dipping than the underlying signal, and much higher frequency. An FK filter is designed to remove the steeply dipping events, and a 50 Hz, zero-phase, low-pass Butterworth filter is used to attenuate the high frequency artifacts. Figure 24a plots the data prior to denoising but with the low pass Butterworth filter applied, Figure 24b plots the DAS data post noise attenuation and after application of the FK and Butterworth filters, and Figure 24c plots the difference between the data in Figures 24a and 24b. The near offset shots with higher signal to noise ratio are mostly unaffected by the denoising, while the signal-to-noise ratio of the far offset shots appears to improve. The denoised, FK and Butterworth filtered data does retain events that appear to be artifacts especially above the first breaks, however the difference between the two datasets (Figure 24 c) does not include these artifacts suggesting

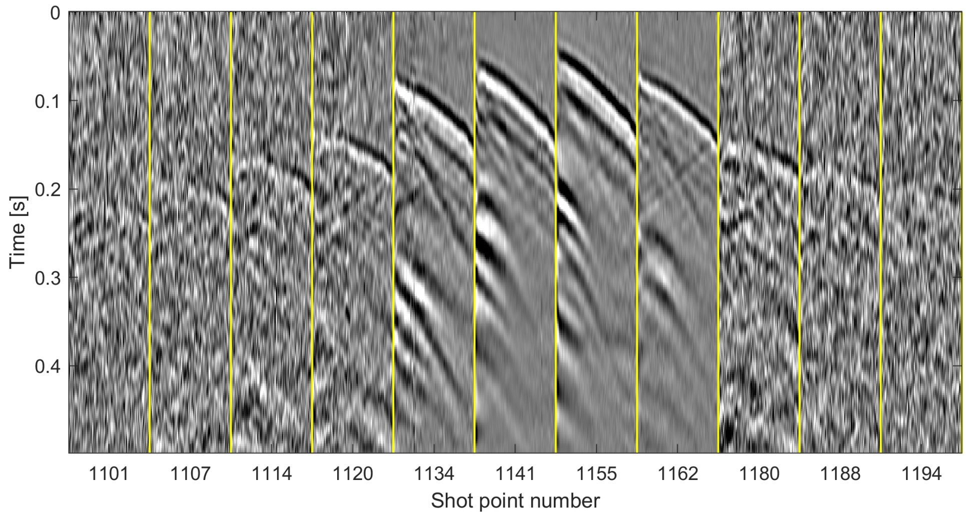

FIG. 22. Depth registered DAS data for every 6^{th} shot point point on source line 1.

that they are also present in the raw data. The difference plot suggests that a majority of the removed energy is Gaussian noise or steeply dipping artifacts. There is still a danger that this workflow has added artifacts that may influence the FWI result, and perhaps it would have been more beneficial to use the dataset prior to noise attenuation for FWI. While the raw data are noisier, they mostly contain Gaussian noise, which FWI is less influenced by then coherent noise and artifacts. If FWI fails to converge on the denoised data, it will be trialed on the noisy dataset.

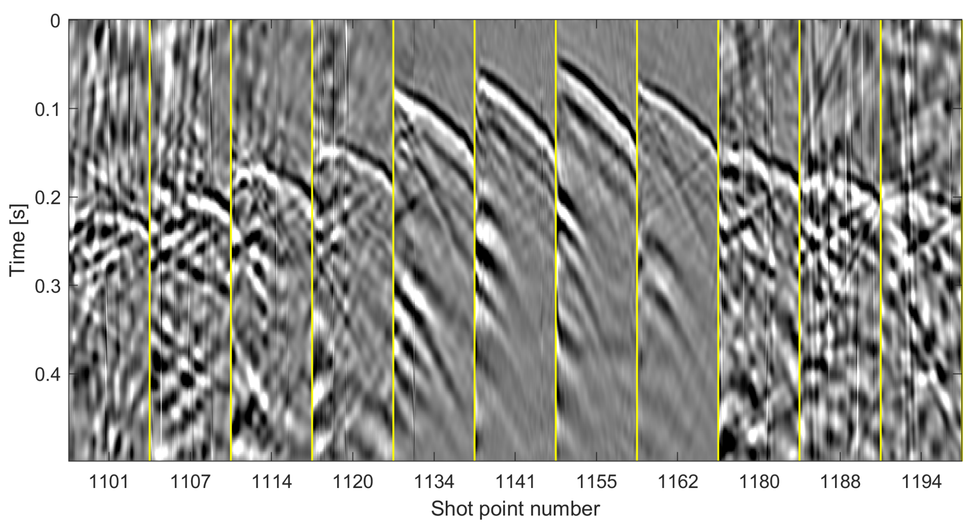

FIG. 23. DAS data after de-noising for every 6^{th} shot point point on source line 1.

After the processing sequence described above, the data were examined for quality control. Shot 1149 (the closest shot to the well), plotted in Figure 25a contains a significant amount of coherent noise between 200 and 300 meters depth that the processing workflow was unable to remove. Analyzing the amplitude spectra for this shot, the coherent noise is observed to exist over a narrow frequency band, so a notch filter is designed by combining

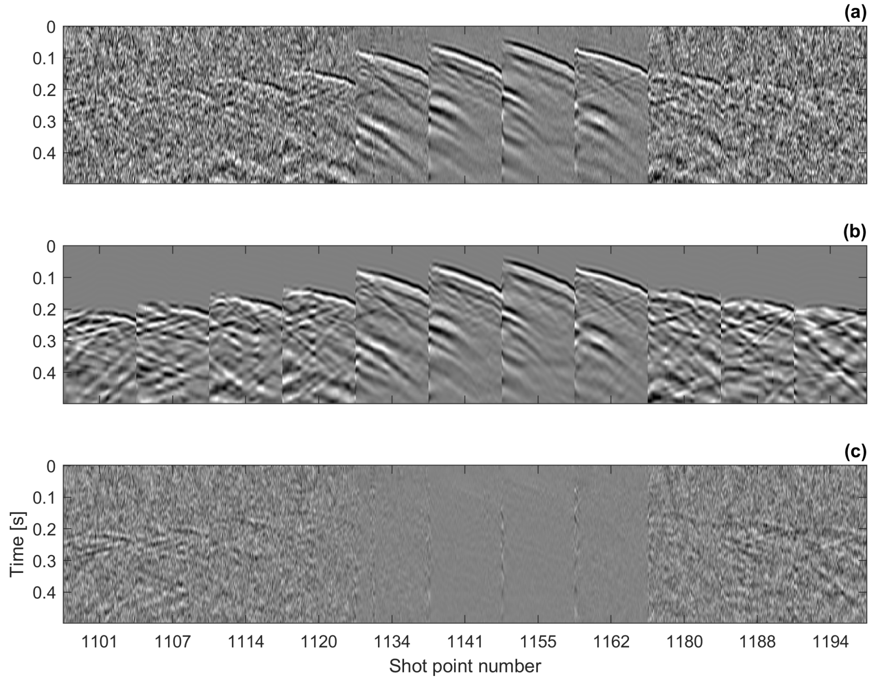

FIG. 24. (a) Raw DAS data low pass filtered to 50 Hz, (b) denoised DAS data after application of the FK and Butterworth filters and muting prior to the first breaks, (c) difference between the datasets in (a) and (b).

low pass (20 Hz) and high pass (30 Hz) Butterworth filters. Figure 25b plots the data after application of this notch filter. Figure 25c plots the mean amplitude spectra before (black) and after (red) notch filtering. The notch filter has significantly attenuated the noise without significantly harming the signal, and has boosted some of the reflection data. However, the band that the notch filter attenuates is crucial for FWI. It is uncertain how the application of the notch filter, and the attenuation over this band will affect FWI. This shot will have to be closely monitored during FWI, and the possibility remains that it may have to be removed from the dataset.After denoising a mute was applied above the first breaks.

DISCUSSION

Full waveform inversion is a powerful technique for estimating subsurface parameter distributions through a data matching procedure. Prior to its inclusion in FWI, measured data must be processed to make them more comparable to simulated data generated by modeling procedures and to remove artifacts from the data. Generally, the most simplistic data processing workflow that serves these two goals is adopted for preparing measured data for FWI. In 2018, CREWES in partnership with the Containment and Monitoring institute acquired a VSP survey with collocated three-component accelerometers, and DAS fiber. In two reports in this issue each dataset is inverted, both in isolation and in combination with each other. To prepare the data for this treatment, in this report we outline the processing steps required for each dataset.

The two datasets are processed with a similar workflow, but inherent differences in each

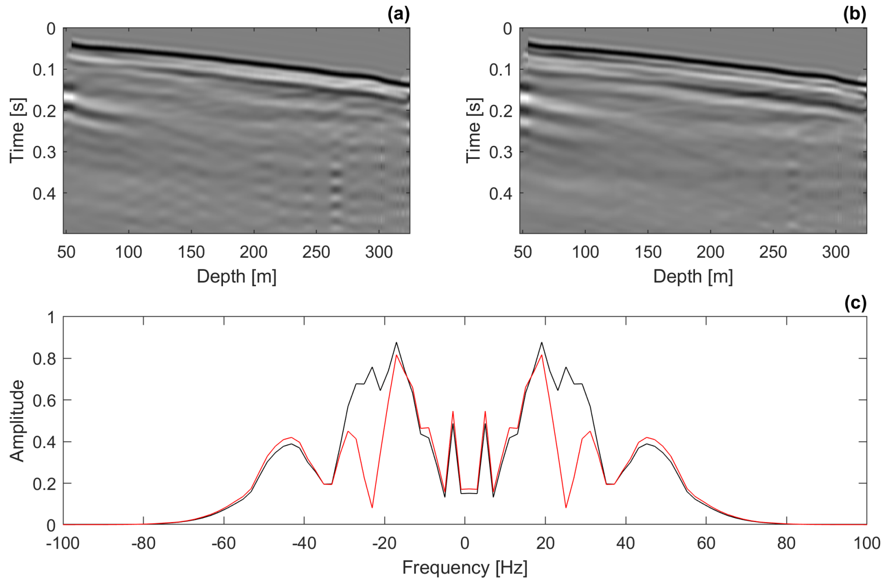

FIG. 25. Shot 1149 from the DAS dataset after (a) application of the processing workflow and (b) after notch filtering. (c) Amplitude spectrum of the data after application of the processing workflow for the intput data (rblack) and filtered data (red).

dataset result in unique steps for each dataset. The accelerometer data is processed using a standard workflow for multi-component VSP data where the goals in this report were to 1) initialize the survey geometry, 2) convert the data to vertical and H_{max} components that are directly comparable to the x and z components of wavefield motion that will be modeled in the FWI reports, and 3) remove noise in the form of dead traces, noisy traces, Gaussian noise, and ringing in the data. The result of this treatment is a high fidelity two-component accelerometer dataset that will be used to support FWI by Keating et al. (2021) and Eaid et al. (2021).

The DAS data underwent a similar processing workflow, but was simplified due to the single component nature of DAS sensing. However, due to uncertainties in the trace spacing, and trace locations in the well, special attention was directed to depth registration of the DAS data. Often a tap test is preformed to initialize the first trace in the well, and the remaining traces are localized using a theoretical trace spacing. This method is prone to error both in locating the first trace, and in uncertainties in the theoretical trace spacing supplied by interrogator parameters. The data driven method presented here is expected to more accurate for depth registration. The reduced signal-to-noise ratio (especially at far-offset) of the DAS data required a more robust treatment of noise attenuation than was required on the accelerometer data. This has potential to introduce artifacts and care must be taken when including the DAS data in FWI. Eaid et al. (2021) discuss the influence placing too much emphasis on DAS data has one the FWI inverted models, and link this back to the reduced signal-to-noise of the far-offset DAS data.

ACKNOWLEDGMENTS

The authors would like to thank the sponsors of the CREWES project as well NSERC under the grant CRDPJ 543578-19 for making this work possible through their financial support. Matt Eaid is partially supported through a scholarship from the SEG foundation. Scott Keating was supported through the Canada First Research Excellence Fund.

The data in this report were acquired through a collaboration with Containment and Monitoring Institute (CaMI) of Carbon Management Canada (CMC). Research at the CaMI field site is supported in part by the Canada First Research Excellence Fund through the Global Research Initiative at the University of Calgary, and the CaMI.FRS Joint Industry Project.

REFERENCES

Cook, J., Nuccitelli, D., Green, S. A., Richardson, M., Winkler, B., Painting, R., Way, R., Jacobs, P., and Skuce, A., 2013, Quantifying the consensus on anthropogenic global warming in the scientific literature: Environmental research letters, **8**, No. 2, 24.

Eaid, M., Keating, S., and Innanen, K., 2021, Full waveform inversion of DAS field data from the 2018 CaMI VSP survey: CREWES Research Reports, **33**, No. 5.

Hall, K., Bertram, K., Bertram, M., Innanen, K., and Lawton, D., 2018, CREWES 2018 multi-azimuth walk-away VSP field experiment: CREWES Research Reports, **30**, No. 16, 1–14.

Isaac, J. H., and Lawton, D. C., 2016, Brooks revisited: CREWES Research Reports, **28**, No. 33, 1–10.

Keating, S., Eaid, M., and Innanen, K., 2021, Full waveform inversion of VSP accelerometer data from the CAMI field site: CREWES Research Reports, **33**, No. 27.

Krebes, E. S., 2019, Seismic Wave Theory: Cambridge University Press, 1 edn.

Kweku, D. W., Bismark, O., Maxwell, A., Desmond, K. A., Danso, K. B., Oti-Mensah, E. A., Quachie, A. T., and Adormaa, B. B., 2017, Greenhouse effect: Greenhouse gases and their impact on global warming: Journal of Scientific research and reports, 1–9.

Lawton, D., 2020, Personal communication.

Lawton, D., Hall, K., and Gordon, A., 2018, Advances in DAS seismic monitoring for CO2 storage: SEG Technical Program Expanded Abstracts 2018, 5500–5500.

Lines, L., 2014, FWI and the âĂIJnoiseâĂİ quandary: CREWES Research Report, **26**, No. 49, 1–6.

Macquet, M., Lawton, D. C., Saeedfar, A., and Osadetz, K. G., 2019, A feasibility study for detection thresholds of CO2 at shallow depths at the CaMI Field Research Station, Newell County, Alberta, Canada: Petroleum Geoscience, **25**, No. 4, 509–518.

Oreskes, N., 2004, The scientific consensus on climate change: Science, **306**, No. 5702, 1686–1686.

Qu, L., and Innanen, K., 2021, Near-surface characterization using surface-wave FWI with fiberoptic data: CREWES Research Reports, **33**, No. 40.

Rodhe, H., 1990, A comparison of the contribution of various gases to the greenhouse effect: Science, **248**, No. 4960, 1217–1219.

Spackman, T. W., 2019, Novel orbital seismic sources at a CO2 storage monitoring site, Newell County, Alberta: M.Sc. thesis, University of Calgary.

Zhao, Q., Du, Q., Gong, X., and Chen, Y., 2018, Signal-preserving erratic noise attenuation via iterative robust sparsity-promoting filter: IEEE Transactions on Geoscience and Remote Sensing, **56**, No. 6, 3547–3560.